Photonic Seismometer Based on Whispering Gallery Modes

Jaime da Silva*[1], Elie R. Salameh[1], M. Volkan Ötügen[1], and Dominique Fourguette[2,3]

Abstract

We present the concept of an all-optical seismometer based on the principle of optical whispering gallery modes (WGMs). The proposed sensor is compact, rugged, low power, and resistant to electromagnetic interference. A cantilever configuration of a fiber-pigtailed photonic integrated circuit with a ring resonator is employed as the sensing element. The measurement approach is based on the optical excitation of the WGMs of a ring resonator using a 1313 nm tunable diode laser. A digital signal processing system analyzes the recorded WGM scans. The base acceleration is calculated from the WGM shifts caused by the deformation of the optical ring resonator. A prototype seismometer is developed, calibrated, and tested. The frequency response of the seismometer is assessed by observing the free vibration of the sensor. The preliminary results are encouraging and suggest that a WGM-based optical seismometer is feasible.

Cite this article as da Silva, J., E. R. Salameh, M. V. Ötügen, and D. Fourguette (2022). Photonic Seismometer Based on Whispering Gallery Modes, *Seismol. Res. Lett.* **XX**, 1–10, doi: 10.1785/0220210253.

Introduction

Seismometers are ubiquitously employed in a wide range of applications on Earth. They have also been used in other planetary explorations as first demonstrated by National Aeronautics and Space Administration's (NASA) Apollo Lunar Surface Experiment Package between 1969 and 1977. Since then, various planetary missions have benefitted from the deployment of seismometers, with NASA InSight being one of the most recent. The Seismic Experiment for Interior Structure (SEIS), as part of the InSight Mars mission, highlights the importance and contribution of seismometers in planetary exploration.

SEIS is considered to be the most advanced seismometer in planetary exploration to date and provides excellent data on the seismic activity of Mars (Clinton *et al.*, 2021). In addition to the three-axis very-broad-band (VBB) inverted-pendulum seismometer acting as its main instrument, the SEIS also includes a compact short-period (SP) microfabricated silicon-based sensor, dedicated to the detection and measurement of higher frequency seismic events in the 0.1–40 Hz band (Lognonné *et al.*, 2019). The inclusion of the SEIS-SP suggests a need for compact and rugged devices in planetary seismology. In addition, the sensitivity to variations in ambient conditions (particularly, pressure and temperature), as observed in both the VBB and the SP instruments (Ceylan *et al.*, 2021), is an issue that could be addressed by a different type of sensor. Although space missions would be the primary benefactor of the development of compact and robust seismometers, Earth-bound applications, such as remote sensing, could also stand to benefit. An integrated optical microseismometer would address the requirements of both Earth applications and planetary missions.

On Earth, most modern seismometers consist of spring-mass active devices employing an electromechanical feedback force unit that prevents the movement of the proof mass. The magnitude of the force required to maintain the mass at rest determines the ground motion. Owing to the closed-loop circuit, the response of the seismometer can be configured to cover a designated band. However, the addition of circuitry introduces both electronic noise and heat generation due to electric power dissipation. Traditional passive seismometers, such as geophones, also require amplifiers to increase the intensity of the generated electrical signal. Optical seismometers present an alternative to electromechanical seismometers because they eliminate the need for electronics near the sensing element. Although there is a variety of laser-based seismometers, interferometric optical seismic sensors present a particularly attractive alternative to their electromechanic counterparts because they employ a different operating principle, rendering them inherently resistant to the same type of undesirable interferences.

Interferometric seismometers

Several interferometric optical seismometers for applications on Earth have been presented by various groups. Zumberge *et al.* (2010) developed an open-loop vertical seismometer based on a Michaelson interferometer. This sensor relies on

1. Mechanical Engineering Department, Southern Methodist University, Dallas, Texas, U.S.A.; 2. Now at SMU and Perikin Enterprises, Albuquerque, New Mexico, U.S.A.; 3. Michigan Aerospace Corporation, Ann Harbor, Michigan, U.S.A.

*Corresponding author: odasilva@smu.edu

the displacement of a mirror attached to the leaf-spring mechanism of a modified STS1 seismometer (Wielandt and Streckeisen, 1982). The iSTS1 (i corresponding to interferometric) seismometer responds to acceleration and was employed for the measurement of ground motion in the Black Forest Observatory (Berger *et al.*, 2014). The Michaelson interferometric technique was also applied in the development of a three-component borehole seismometer. This sensor was deployed in the Albuquerque Seismological Laboratory and used to measure an earthquake (Zumberge *et al.*, 2018). The outputs of the presented interferometric seismometers show good agreement with more established instruments, such as STS1 (Zumberge *et al.*, 2010), STS2 (Berger *et al.*, 2014), and KS-54000 (Zumberge *et al.*, 2018) seismometers.

Motivated by the promising preliminary work of Zumberge *et al.* (2003), a group at the Institut de Physique du Globe de Paris developed a Fabry-Pérot-based optical geophone as part of the Laser Interferometry for Earth Strain (LINES) project (Bernard *et al.*, 2019). This device consists of a modified SP geophone (2 Hz) with a mirror attached to its mobile mass. An optical fiber transmits a light beam that is reflected by the mirror and injected back into the fiber to generate an interferometric signal. The ground motion is determined from the phase difference of two signals, obtained by demodulating the interferometric fiber signal using a dedicated signal processing circuit. Through this project, a 3D LINES geophone was successfully employed for remote measurement of ground motion (velocity) on the seafloor. Owing to its optical characteristics, this sensor proves to be low noise and highly sensitive, capable of resolving velocities as small as 12 pm/s (noise floor) with a dynamic range of 28 bits (based on 2 mm/s velocity cutoff). Although the LINES seismometer offers good performance, it requires the geophone to be protected from corrosion of its metallic components due to atmospheric humidity. In addition, the reliance on a long stretch of optical fiber to generate the optical interference makes the approach susceptible to external conditions. A more direct interferometric measurement approach may be achieved using a resonant optical cavity, such as a whispering gallery mode (WGM), as presented in this work.

WGM sensors based on optical mode shifts are shown to be effective for seismic applications such as that presented in U.S. patent number 8743372 (Fourguette *et al.*, 2014). This approach relies on the resonant frequency shift of the optical modes of a fiber-coupled dielectric microsphere (1500–200 μm in diameter). Unlike the previously discussed interferometric sensors, resonance is generated in an optical cavity when a given set of conditions are satisfied. These optical resonances are observed as sharp dips in the transmission spectrum of the fiber coupled to the resonator as most of the optical energy is contained in the resonator. A leaf-spring-mass system is used to modify the shape of the microsphere, leading to a resonant optical frequency (WGM) shift. The ground motion (acceleration) is determined by tracking the location of the WGMs. This device is compact, lightweight, and low power, capable of resolving acceleration in the order of 1 ng with a dynamic range of 10 bits (Fourguette *et al.*, 2012). Despite its successful implementation, the sensor is limited by the mechanical weakness of the fiber-to-resonator coupling, which impedes its potential use in the field. The sensor proposed in the present is the next-generation implementation of the one presented in US8743372. The core optical element is an on-chip waveguide-coupled ring resonator (as opposed to a fiber-coupled sphere resonator). Its monolithic design allows for a rugged sensor suitable for field deployment.

Optical seismometers offer various benefits over their electromechanical counterparts. Because the sensing element consists of dielectric materials, the influence of electromagnetic interference is significantly reduced. In addition, optical seismometers connected by low-loss fiber networks can be deployed at great distances from the optoelectronic processing systems (Bernard *et al.*, 2019). The all-optical fiber input-output connections allow for this class of sensors to be multiplexed into seismometer networks. Finally, the versatility of WGM sensing allows for the employment of other optical reference sensors designed to compensate for the variations in ambient conditions (e.g., temperature or pressure) that can affect the output signal (Salameh *et al.*, 2021).

WGM-based seismometers with large optical quality factors (Q_{op}) can offer high-measurement resolutions. The sensing capabilities of high-Q_{op} resonators are demonstrated by a force sensor with a resolution of 1 pN (Ioppolo *et al.*, 2009). Given their sensing potential, WGM resonators present an attractive solution for applications requiring high-measurement resolution such as seismology.

In this work, we present the concept of an all-optical cantilever-based WGM seismometer. Static and dynamic characterizations of a prototype seismometer are performed to assess the sensitivity and response. The results from the sensor calibration, supported by computational models, are discussed. An additional experiment demonstrating the potential of an in-house microfabricated cantilever is also presented. All the results are obtained in laboratory conditions.

Seismometer Concept

Measurement principle

The concept of WGM was first mathematically formulated by Lord Rayleigh in the nineteenth century to describe the frequency-selective propagation of sound waves along the concave surface of a solid wall (Rayleigh, 1910). Since then, the same phenomenon has also been observed for electromagnetic waves on curved optical cavities, often referred to as optical WGM. For a circular cavity, the geometric formulation of WGM yields a resonant condition given by

$$2\pi R n = l\lambda, \tag{1}$$

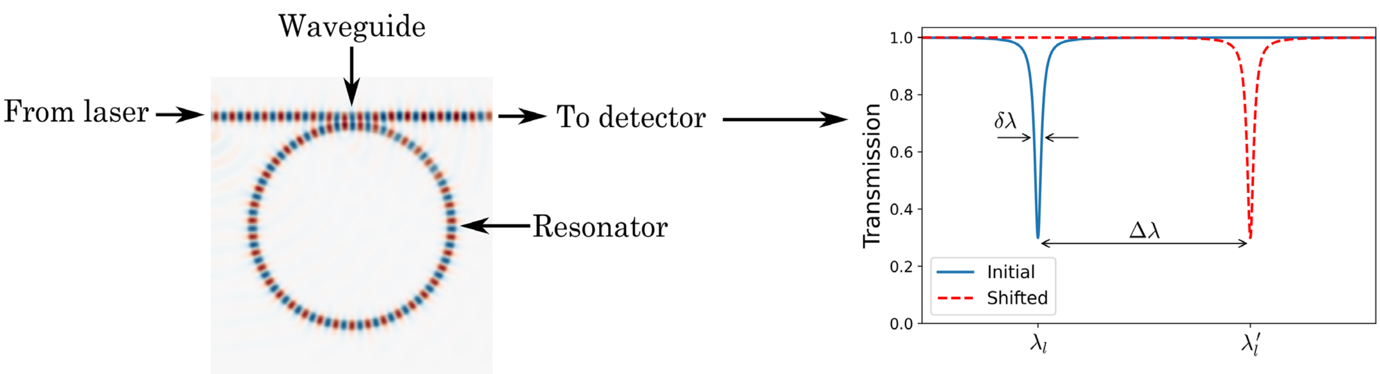

Figure 1. Snapshot of a simulation of a waveguide-coupled ring resonator undergoing whispering gallery mode (WGM) excitation and an idealized transmission spectrum depicting mode shift. The color version of this figure is available only in the electronic edition.

in which R, l, n, and λ are the radius of the resonator, polar mode number (integer), the effective refractive index of the optical mode, and resonating wavelength, respectively. This expression is only a first-order approximation of the resonant condition but is sufficiently accurate for $R \gg \lambda$.

Equation (1) indicates that the resonance depends on R and n, so changes in the morphology of the resonator lead to a shift of the resonant wavelength. This dependence is expressed as

$$\frac{\Delta\lambda}{\lambda} = \frac{\Delta R}{R} + \frac{\Delta n}{n}. \tag{2}$$

In the current application, the contribution to the WGM shift from the effective refractive index (photoelastic effect) is negligible as the mode shift is dominated by the effect of the mechanical strain ($\Delta R/R$). Multiple strain-based WGM sensors are demonstrated in the literature for the measurement of quantities such as pressure (Ioppolo and Ötügen, 2007), force (Ioppolo *et al.*, 2008), temperature (Guan *et al.*, 2006), and acceleration (Ioppolo *et al.*, 2011). The versatility of this class of sensors makes them attractive for a wide range of applications.

When light from a tunable laser is injected into a waveguide that is evanescently coupled to a ring resonator, the WGMs are observed as sharp dips in the transmission spectrum, as shown in Figure 1. The mode shift ($\Delta\lambda_{\mathrm{res}}$) and the resonance linewidth ($\delta\lambda$) are obtained by observing the transmission spectrum. The optical quality factor, defined as

$$Q_{\mathrm{op}} = \frac{\lambda}{\delta\lambda}, \tag{3}$$

is associated with the resolution of the resonator as a sensor. Narrower dips (higher Q_{op}) allow for the detection of smaller mode shifts and, hence, higher sensor resolution.

In our analysis, we define the lower limit of detection as the root mean square (rms) noise of the mode shift. For the present sensor, the anticipated dominant sources of measurement uncertainty are related to equation (2): thermal noise due to the large thermo-optic coefficient of the resonator material, shot noise, and quantization noise introduced through digitization of the signal.

As shown in Figure 2a, the proposed sensor operates based on the deformation of a ring resonator embedded in a silicon substrate. The chip with the ring resonator has a cantilever section, and a proof mass attached to the tip (shown in the photograph in Fig. 2b). The chip carrier shown is attached to a base for which motion is monitored. For an Euler–Bernoulli cantilever beam, the strain is defined as (Park and Gao, 2006)

$$\epsilon_{xx} = -z\frac{d^2w(x)}{dx^2}, \tag{4}$$

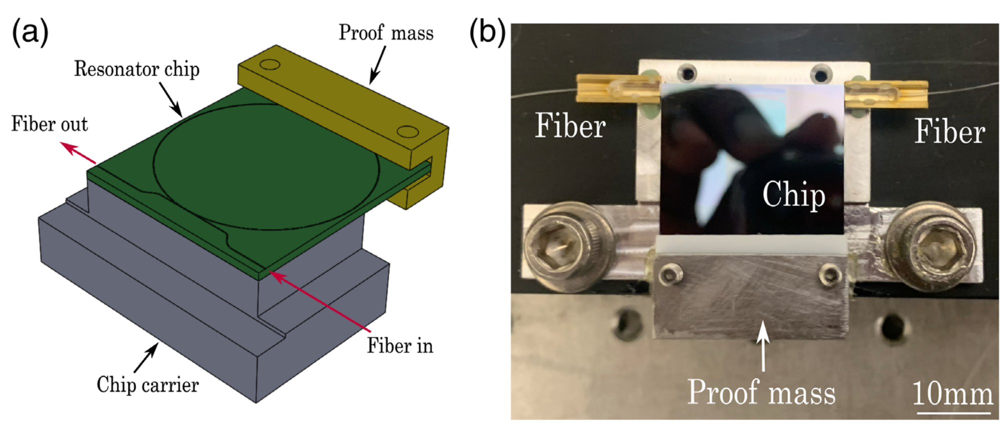

Figure 2. (a) Three-dimensional rendering of the sensing element and (b) a photograph of the prototype (top view). The color version of this figure is available only in the electronic edition.

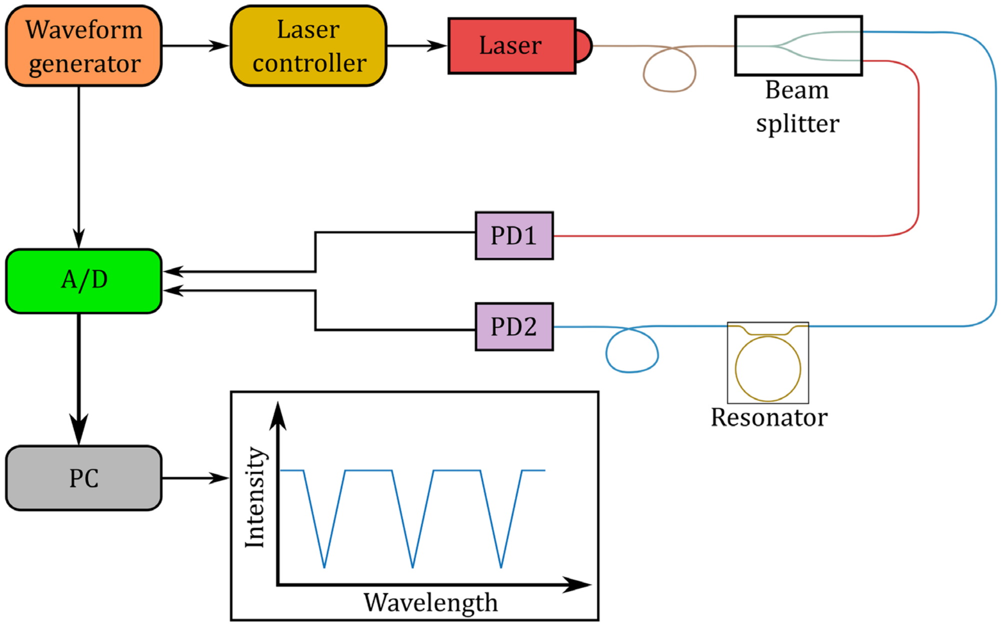

Figure 3. Schematic of the sensor system. The color version of this figure is available only in the electronic edition.

in which x is the coordinate along the length of the beam and z is the transverse distance from the neutral axis (zero stress plane) of the beam. The function $w(x)$ is the deflection of the beam caused by the transverse load (P) at the free end:

$$w(x) = \frac{Px^2}{6EI}(3L - x), \tag{5}$$

in which E, I, and L are the Young's modulus, the area moment of inertia, and the length of the beam overhang, respectively.

The ring resonator, embedded in the cantilever beam, essentially acts as a strain gauge that monitors the deflection of the beam due to an applied load. In the present, the load P is generated by the acceleration of the proof mass. Equations (4) and (5) show that the local strain is linearly proportional to the load for small deflections. For cantilever beams, the equation of motion can be expressed in terms of the tip displacement $y = w(L)$ relative to the motion of the base as

$$\ddot{y} + \frac{\omega_n}{Q_m}\dot{y} + \omega_n^2 y = -\ddot{u}, \tag{6}$$

in which ω_n, $\ddot{u}$, and Q_m are the natural frequency of the first vibrational mode of the undamped beam, the acceleration of the base, and the mechanical quality factor of the system, respectively. It can be shown that the strain expressed as the first term on the right side of equation (2) is linearly proportional to the tip displacement. Hence,

$$y = A\frac{\Delta\lambda}{\lambda}, \tag{7}$$

in which A is a constant. Therefore, the motion (acceleration) of the base can be determined directly from the WGM shift.

As indicated in equation (6), the response of the system to the motion of the base to which it is attached is described by parameters Q_m and ω_n. The vibration of mechanical structures typically involves damping related to multiple loss factors that affect Q_m. The combined effect of loss mechanisms can be estimated from

$$\frac{1}{Q_m} = \frac{1}{Q_{\mathrm{TE}}} + \frac{1}{Q_{\mathrm{air}}} + \frac{1}{Q_{\mathrm{bulk}}} + \frac{1}{Q_{\mathrm{other}}}. \tag{8}$$

The terms on the right side of equation (8) represent losses due to the thermoelastic effect, air–beam interaction, internal material friction, and other factors (e.g., beam-to-clamp energy transfer). Most of these losses are negligible owing to their high Q (typically 10^4–10^9). For instance, Blom *et al.* (1992) report that the Q_{bulk} of silicon is 2×10^5. In addition, using Blom's model for the viscous regime (Sumali and Carne, 2007), Q_{air} is estimated to be $\sim 10^6$. However, it should be noted that the optical chip is attached to the carrier (see Fig. 2) by a layer of epoxy which contributes to Q_m. With a reported $Q_{\mathrm{bulk}} = 27.2$ (Mansour *et al.*, 2016), the contribution from this layer could potentially dominate over other loss factor effects in determining Q_m.

Sensor system

As shown in Figure 2, the sensing element consists of an optical chip positioned as a cantilever plate with an embedded waveguide and ring resonator. The chip is fiber-pigtailed to facilitate the coupling of light into and out of the waveguide. A section of the bottom face of the chip is affixed to an aluminum carrier, resulting in an overhang (cantilever), to which the proof mass is attached.

The optical chip is composed of a silicon substrate with a thin silica layer at the top. The silicon nitride waveguide and ring resonator are embedded in the silica layer. The dimensions of the chip are 27 mm × 25 mm × 1 mm ($L \times W \times H$). The resonator overhang is 11 mm, and the radius of the resonator is 12 mm.

Figure 3 illustrates the optoelectronic configuration for the sensor prototype. A waveform generator (1 kHz ramp) is used to modulate the wavelength of the light emitted by a continuous wave 1313 nm distributed-feedback (DFB) diode laser. The DFB laser is an off-the-shelf unit commonly used in the telecommunication industry. The laser light is divided into two through a 90:10 in-fiber beam splitter, and the 90% channel feeds the chip to excite the WGM. The output light from the chip is coupled to photodetector PD2. Similarly, the 10% light is coupled to detector PD1 and serves as a reference to remove the modulation profile from the WGM signal. All signals are acquired by 12-bit analog-to-digital (A/D) converter. The modulation signal is also used to trigger and synchronize the acquisition of the photodiode signals. A personal computer connected to the A/D converter is used to record the data for signal processing.

Signal processing

Although real-time signal processing has been previously demonstrated for high-speed transient WGM sensing (Ali *et al.*, 2015), we choose a postprocessing approach that allows us to perform various analyses on the data, as well as develop and compare different signal processing techniques.

Three approaches were considered for signal processing: dip detection (DD), cross correlation (CC), and Lorentzian fitting (LF). The simplest approach DD consists of tracking the location of the minimum of the resonance dip signal. In the CC approach, a reference and a shifted WGM dips are cross correlated, and the mode shift is determined from the location of the peak of the correlation output (Ali, 2015). Finally, the LF method, which is the most computationally demanding, relies on the fitting of a Lorentzian function to a WGM dip to estimate the center and width of the resonance. Although DD is the fastest algorithm, it is also the most susceptible to noise because it only tracks the location of the minimum of the signal which can exhibit dithering. The CC algorithm exhibits better performance, with lower noise than DD, but at the expense of increased computation time. Finally, LF is considered to be the most robust algorithm because it uses the overall profile of the resonance instead of a single point. However, this is at the expense of computation time and resources because it is an iterative process. For real-time applications, both DD and CC are suitable, with CC being favored because it can be easily configured for measurements exceeding the free-spectral-range of the ring resonator (Ali, 2015). Hardware realizations of CC circuits are also possible (Baloch *et al.*, 2014), which would reduce the computational demand of the envisioned seismometer.

Results

The sensing element is characterized using several approaches. A static analysis is first used to assess the force sensitivity of the resonator. The sensor is then tested in a series of dynamic experiments: harmonic excitation on a vibration table, and impulse perturbation, with and without damping. The instrument's sensitivity, resolution, and frequency response are determined from these results.

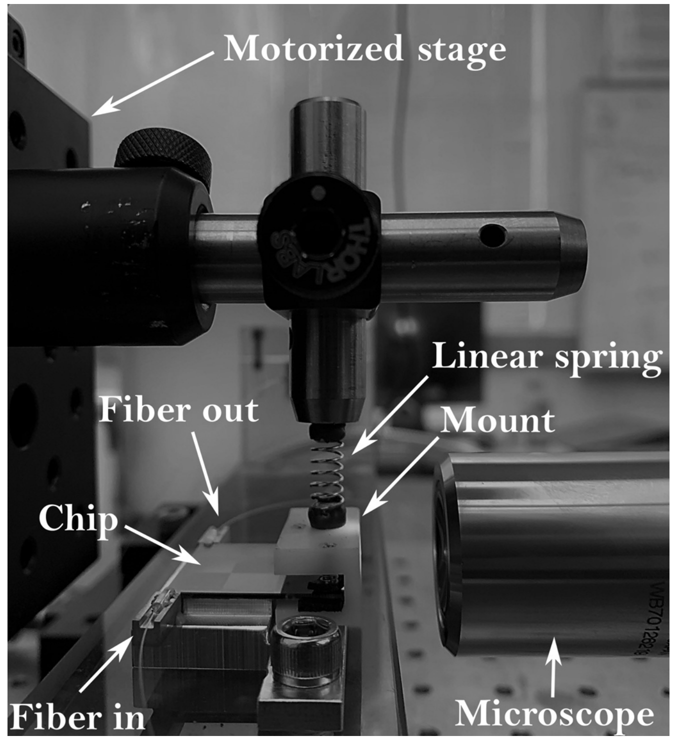

Figure 4. Apparatus employed for the determination of static force sensitivity.

Static characterization

The apparatus shown in Figure 4 is used to deform the optical chip and measure the tip deflection. A linear spring attached to a motorized nano-translation stage is used to generate the force. The force magnitude is determined from the displacement of the translation stage (compression of the spring). A plastic mount is used to transfer the spring force onto the chip.

Figure 5a shows the movement of WGM in the transmission spectrum caused by the applied force. The reference wavelength (λ_r) is the initial location of the WGM dip. The resonance shift depends on the magnitude of the force. The location of the resonances is tracked by an LF algorithm that also provides an estimated optical quality factor ($\sim 1.5 \times 10^7$ at present).

Figure 5b shows the dependence of the WGM shift on the applied force. Computational estimates of the mode shifts are also shown in the figure. Given that equations (4) and (5) apply to 1D beams, for a more accurate model the computations are performed using 3D finite-element analysis (FEA) of the same geometry used in the experiments. The WGM shifts are calculated by computing the change in the perimeter of a circle located on the top surface of the plate. The perimeter of the closed line before (L_i) and after (L_f) deformation is determined through the corresponding line integral ($\oint dl$). The change in the perimeter is related to the WGM shift by

$$\Delta\lambda = \lambda \frac{L_f - L_i}{L_i}. \tag{9}$$

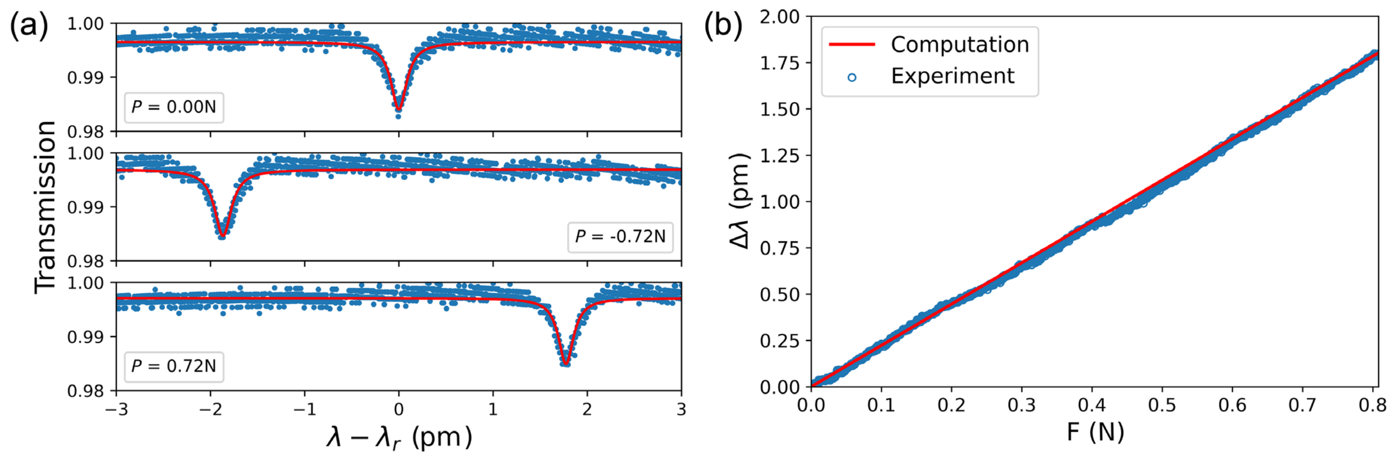

Figure 5. (a) Shift of optical resonance (WGM) due to an applied force and (b) measured WGM shift as function of the applied force. The color version of this figure is available only in the electronic edition.

The ratio $(L_f - L_i)/L_i$ represents the total strain on the resonator. The estimated shift-force sensitivity is 2.23 pm/N. The FEA model also shows that the tip displacement and the effective strain on the resonator have a linear relationship, thus the motion of a proof mass attached to the free end of the plate can be determined from the mode shift.

Harmonic excitation

A vibration table is used to calibrate the acceleration of the seismometer following the procedure described in Wielandt (2012). The setup for this experiment is shown schematically in Figure 6. The prototype seismometer and a commercial MEMS accelerometer are attached to a base, which is rigidly connected to the vibration table. The motion of the table is controlled by a harmonic signal from a waveform generator (15 Hz sinusoidal waveform). The accelerometer serves as a reference scale for calibration. In this preliminary experiment, a 25 g proof mass is used and no damping is employed.

The laser is scanned at a rate of 1 kHz and the transmission spectrum is acquired at 5 k samples per cycle of the laser (or 5 MSamples/s), which is sufficient to resolve the WGM dips. Each scan of the laser yields a single point in the time evolution of the WGM shift, resulting in 67 WGM data points per cycle of the shaker table oscillation.

The time variation of the WGM shift and the corresponding accelerometer output is shown in Figure 7a. The result shows the efficacy of monitoring acceleration by tracking WGM shifts. The harmonic motion of the base results in a harmonic shift of the WGM. The phase difference between the two signals is attributed to the distinct mechanical impedances of the two systems. The two signals are aligned by a CC-based algorithm, and the mode shift is plotted against the measured acceleration of the table in Figure 7b. The linear fit yields a sensitivity of 1.97 pm/m/s^2, with a 2% rms error (or 0.062 m/s^2). The relatively low sensitivity of the seismometer is due to the large stiffness of the 1-mm-thick substrate used in the present preliminary setup. The sensitivity may be increased by adjusting various parameters in the sensor design, including increasing the proof mass weight, using a more compliant substrate, adjusting the substrate material, thickness, and overhang length.

Free vibration

The system parameters in equation (6) for the prototype sensor were determined using an impulse response experiment. An impulse force was applied to the proof mass, disturbing it from its rest position. The response of the sensor was observed by monitoring the WGM shift. Figure 8a shows the optical mode shift due to the perturbation of the proof mass. The free vibration solution of equation (6) is

$$y(t) = y_0 e^{-\omega_n t/2Q_m} \sin(\omega_d t + \phi_0), \tag{10}$$

in which $\omega_d = \omega_n \sqrt{1-(2Q_m)^{-2}}$ is the damped frequency. The displacement amplitude y_0 and phase ϕ_0 depend on the initial displacement and velocity. These parameters are used as inputs to a least-squares-fit algorithm applied to equation (10). The WGM shift fitting yields the plot in Figure 8b. The corresponding Q_m and ω_n are 26.6 and 136 Hz, respectively. The harmonic

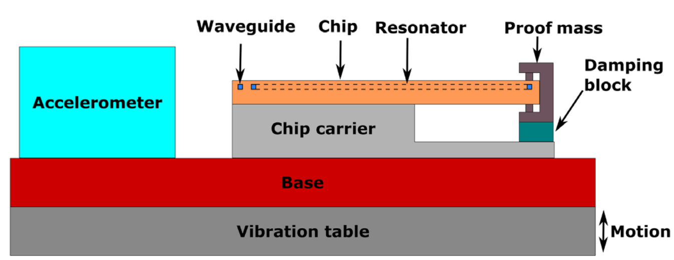

Figure 6. Schematic of the shake table experiment. The color version of this figure is available only in the electronic edition.

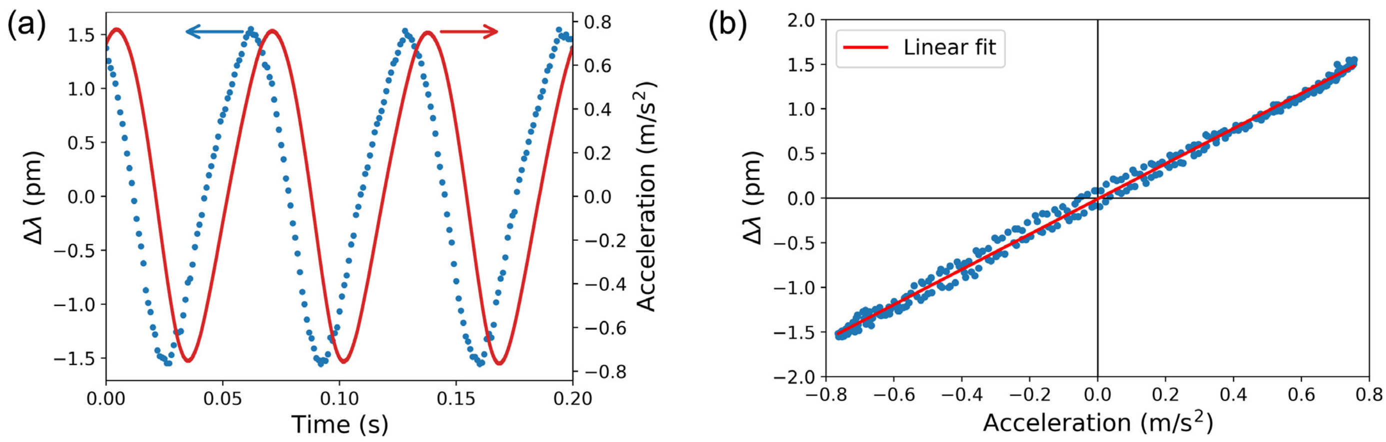

oscillator model shows good agreement with the experimental observations.

The frequency response of a harmonic oscillator due to an impulse input is given by

$$|Y(\omega)| = \frac{B}{[(\omega^2 - \omega_n^2)^2 + (Q_m^{-1}\omega\omega_n)^2]^{\frac{1}{2}}}, \tag{11}$$

in which B is a constant that accounts for the magnitude of the perturbation and has units of acceleration. Figure 8c shows the amplitude as a function of the frequency. The figure indicates that the response of the sensor is flat below 40 Hz but the amplitude increases sharply and significantly at resonance, which is not a desirable trait for a seismometer, even though the seismic input can be calculated from the transfer function of the sensor. Therefore, damping approaches suitable for the present configuration need to be considered for future versions of the seismometer. However, the present preliminary results show the viability of the cantilever substrate, with an embedded ring resonator, as a miniature photonic seismometer.

Resolution and dynamic range

The sensor resolution can be estimated from the WGM shift noise floor and sensitivity. For the current prototype, the

Figure 7. (a) Measured WGM shift (dots) and acceleration of table (solid line) and (b) phase-corrected plot of WGM versus measured acceleration. The color version of this figure is available only in the electronic edition.

WGM shift rms noise, in the absence of a proof mass and any mechanical excitation, is 4.94 fm for a laser scanning rate of 200 Hz, which corresponds to 2.5 $\mathrm{mm/s^2}$ based on the sensitivity of 1.97 $\mathrm{pm/m/s^2}$ (Fig. 7b). This scanning rate is selected to be comparable to the bandwidths of the SEIS-SP and mainstream geophones such as the SM-24.

The dynamic range is limited by the elastic range of the beam. In the current configuration, the seismometer does not have mechanical stops to prevent the excessive deformation of the beam, but once added the goal would be to constrain the motion to avoid plastic deformation. Namazu *et al.* (2000) reported an average bending strength of 470 MPa for millimeter-scale Si cantilevers. Based on this information, a reasonable limit for the present cantilever is 235 MPa (50% safety factor), corresponding to a maximum shift of 143 pm based on a numerical beam model accounting for geometric nonlinearities (i.e., large deformation). Using the rms noise as the measurement resolution, the estimated dynamic range is

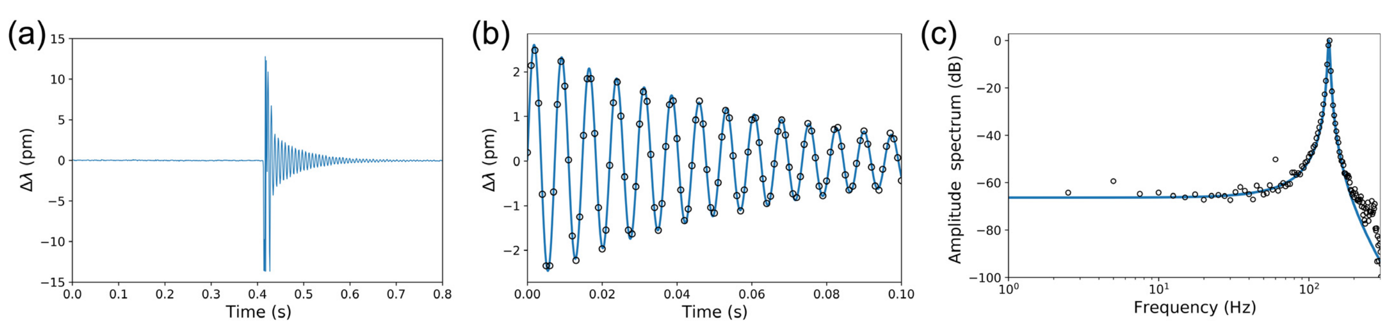

Figure 8. (a) Free vibration of prototype sensor with part of the signal prior to the perturbation, (b) ring down fitting of equation (10) (solid line) and experimental values (circles), and (c) peak-normalized amplitude response from experiment (circles) and equation (11) with estimated parameters from equation (10) (solid line). The color version of this figure is available only in the electronic edition.

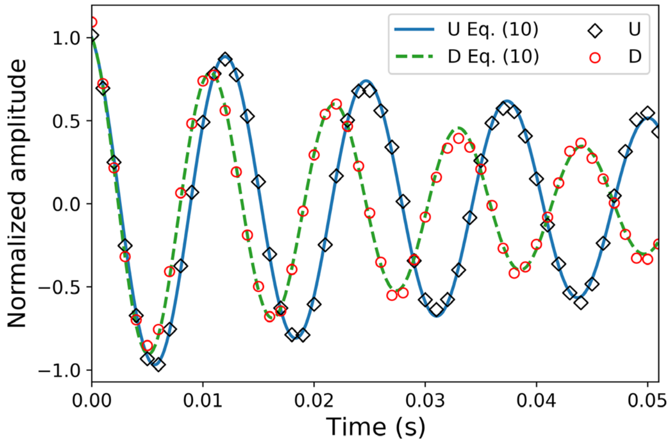

Figure 9. Normalized amplitude of sensor with (D) and without (U) damping. The color version of this figure is available only in the electronic edition.

90 dB. Improvements on the dynamic range can be achieved by reducing the sensor noise floor (e.g., using larger Q_{op} resonators) and increasing the sensitivity by selecting different substrate materials and optimizing the proof mass.

Damping

The results presented earlier for the current silicon cantilever prototype show that the sensor has very low intrinsic damping. Therefore, additional damping needs to be integrated into the system for improved performance. In the present study as an initial attempt, a 1-mm-thick polydimethylsiloxane (PDMS) slab is added between the proof mass and the chip carrier to flatten the resonance (see Fig. 6). The PDMS block has a 20:1 base-to-curing-agent mass ratio with a loss tangent of 0.2–0.5 (Rubino and Ioppolo, 2016). Figure 9 shows the free vibration of the sensor with a 70 g proof mass with and without the damping block. When the damping is added, Q_m decreases from 17.5 to 11.5, whereas ω_n shifts from 79 to 90 Hz.

Although the damping structure improves the response of the system, it does so at the expense of sensitivity. This can be attributed to the relation between the loss tangent and the complex Young's modulus (storage and loss) of the material, which factors into the displacement term of equation (6). Soroka (1949) provides a model in which the structural damping ($\eta = 1/Q_{bulk}$) is represented by a complex spring stiffness and shows that increasing η leads to slightly higher (less than 1%) damped natural frequencies. However, in our experiment, the observed large shift in natural frequency (∼13%) is primarily due to the introduction of the damping block leading to a larger overall stiffness. Although this effect could be mitigated by increasing the mass to prevent loss of sensitivity, different damping approaches should also be investigated for an enhanced sensor design.

Alternatives to hysteretic damping could flatten the mechanical resonance (Fig. 8c) without significantly affecting the sensitivity. The squeeze film effect (Bao and Yang, 2007) presents an attractive solution for the present sensor because it does not require the addition of new components, but rather an improved geometric design. Alternatively, placing the sensing element in a pressurized air container could improve the viscous damping (Sumali and Carne, 2007), but practical considerations are necessary to ensure no pressure leakage from the sensor enclosure. These damping mechanisms would greatly improve the performance of our sensing element while allowing it to remain passive.

Computations on a Raspberry Pi 4

The proposed sensor's primary target application is remote sensing where computational resources are limited. Therefore, it is necessary to assess the computational requirements for effective sensor performance. For this purpose, a Raspberry Pi 4 is employed to compute the WGM shifts of the signals previously recorded by the A/D in Figure 3. The signal processing algorithms discussed earlier are tested. The results show good agreement among all three approaches, with an average computational time close to the sampling period of the WGMs (∼1 ms). This suggests that the WGM shift can be determined in pseudo-real-time, either by a dedicated digital or analog circuit, or a minicomputer such as the Raspberry Pi.

Thin SiO_2-Si-SiO_2 beam

In the present demonstration, the 19-μm-thick SiO_2 optical layer (with the bus waveguide and the ring resonator) is grown over a commercially available 1-mm-thick silicon (Si) substrate. For a given proof mass, the sensitivity of the cantilever system can be improved using thinner Si substrates. To demonstrate the sensitivity potential of the current sensor approach, a preliminary plate is fabricated in-house to have a lower stiffness. The plate consists of a 110-μm-thick Si substrate with an 8 μm silica layer grown on each side, one of which would house the waveguide resonator. Figure 10a shows a scanning electron microscope photograph of the cross-section of a representative sample plate.

The testing configuration in Figure 10b is used for the dynamic characterization of the plate. Light from a 640 nm continuous-wave laser is reflected from the surface of the sample to an optical position detector. The free vibration of the system is measured by disturbing the plate and recording the signal from the detector. The dimensions of the plate are 3 cm × 1 cm × 126 μm with a 2.5-cm-long overhang. A 230 mg proof mass is added at the free end of the beam. The peak normalized frequency response is plotted in Figure 11 alongside a fit of equation (11) with $Q_m = 88$ and $\omega_n = 59.4$ Hz.

The performance of the thin plate seismometer is assessed by a computational model. The geometry employed is the same as the one in the previous experiments, and the ring resonator is represented by a circular line added on the top surface of the

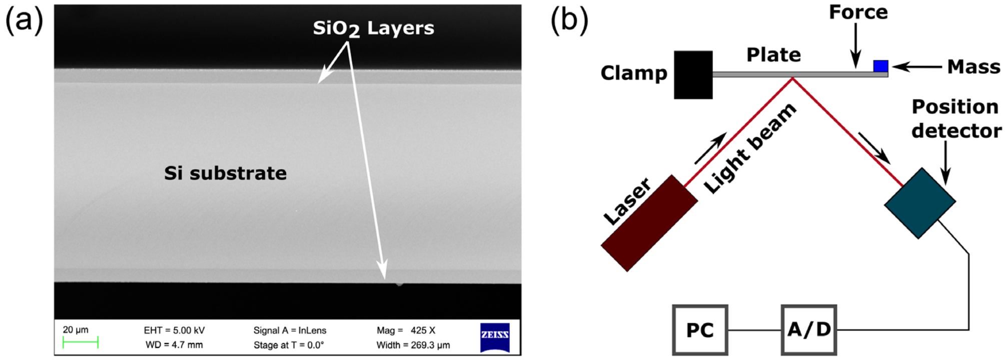

Figure 10. (a) Cross section of a representative beam sample and (b) schematic of apparatus used to measure the response of the thin plate. The color version of this figure is available only in the electronic edition.

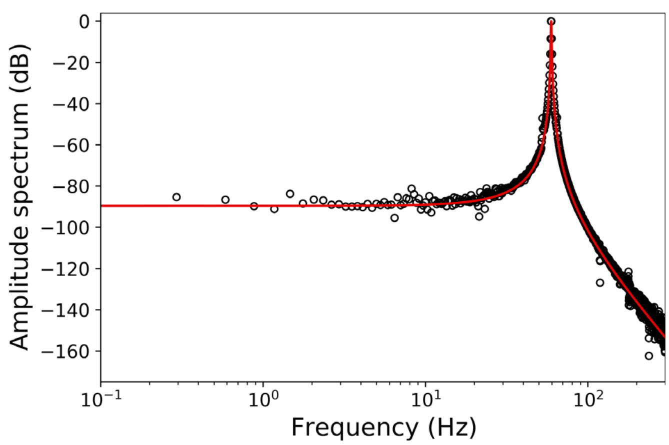

Figure 11. Amplitude spectrum of thin cantilever: experimental values (circles) and equation (11) fitting (solid line). The color version of this figure is available only in the electronic edition.

plate as previously described. For the static case, force is applied on the free end, whereas for the dynamic test, an acceleration is applied to the clamped section of the plate. The calculated force and acceleration sensitivities are 5.5 nm/N and 2.42 $\mathrm{pm/m/s^2}$, respectively. Owing to its lower stiffness, the thin-plate sample performance is superior to that of the 1-mm-thick plate. Thus, soft substrates should be employed to develop highly sensitive sensing elements that allow us to potentially target small-magnitude seismic events in different frequency bands.

Conclusion

We demonstrate the concept of an all-optical cantilever-based seismometer that employs an integrated optical ring resonator. The acceleration of the base is determined from the WGM shift of the embedded resonator. The sensor behaves like a harmonic oscillator, with system parameters estimated by observing the free vibration of the system. The sensitivity can be greatly improved by employing a more compliant microfabricated resonator substrate. Computations on a Raspberry Pi 4 indicate that the sensor works well with low-computational cost signal processing techniques, which is encouraging for remote sensing.

The current prototype sensor is a proof-of-concept of a microresonator-based seismometer. Investigation of a sensor with improved optomechanical performance will be carried out in future work, with the goal of developing a rugged, compact, and versatile seismometer that can be used in both Earth and planetary applications. The compatibility of our sensor with modern microfabrication technologies, such as lithography and chemical vapor deposition, makes it a strong candidate for inexpensive and large-scale production that could allow us to build a package of different types of sensors.

Data and Resources

No data were used in this article.

Declaration of Competing Interests

The authors acknowledge that there are no conflicts of interest recorded.

Acknowledgments

The authors gratefully acknowledge the support from National Aeronautics and Space Administration (NASA) Glenn Research Center (80NSSC17K0519) as part of the COLDTech effort under the guidance of Carolyn Mercer and Mary Voytek.

References

Ali, A. R. (2015). Dielectric micro-resonator-based opto-mechanical systems for sensing applications, *Ph.D. Thesis*, Southern Methodist University, Dallas, Texas.

Ali, A. R., V. Ötügen, and T. Ioppolo (2015). High data rate transient sensing using dielectric micro-resonator, *Appl. Optic.* **54**, no. 23, 7076–7081, doi: 10.1364/AO.54.007076.

Baloch, S., F. Ghazali, N. Mir, F. Farrukh, H. Ismail, and M. Y. Qadri (2014). Hardware realization of locally normalized cross correlation algorithm, *The 2014 2nd International Conf. on Systems and Informatics (ICSAI 2014)*, 378–382, doi: 10.1109/ICSAI.2014.7009318.

Bao, M., and H. Yang (2007). Squeeze film air damping in MEMS, *Sensors Actuators Phys.* **136,** 3–27, doi: 10.1016/j.sna.2007.01.008.

Berger, J., P. Davis, R. Widmer-Schnidrig, and M. Zumberge (2014). Performance of an optical seismometer from 1 μHz to 10 Hz, *Bull. Seismol. Soc. Am.* **104,** no. 5, 2422–2429, doi: 10.1785/0120140052.

Bernard, P., R. Feron, G. Plantier, A. Nercessian, J. Couteau, A. Sourice, M. Feuilloy, M. Cattoen, H.-C. Seat, P. Chawah, *et al.*

(2019). Onland and offshore extrinsic Fabry–Pérot optical seismometer at the end of a long fiber, *Seismol. Res. Lett.* **90,** no. 6, 2205–2216, doi: 10.1785/0220190049.

Blom, F. R., S. Bouwstra, M. Elwenspoek, and J. H. J. Fluitman (1992). Dependence of the quality factor of micromachined silicon beam resonators on pressure and geometry, *J. Vac. Sci. Technol. B* **10,** no. 1, 19–26, doi: 10.1116/1.586300.

Ceylan, S., J. F. Clinton, D. Giardini, M. Böse, C. Charalambous, M. vanDriel, A. Horleston, T. Kawamura, A. Khan, G. Orhand-Mainsant, *et al.* (2021). Companion guide to the marsquake catalog from InSight, Sols 0–478: Data content and non-seismic events, *Phys. Earth Planet. In.* **310,** 106597, doi: 10.1016/j.pepi.2020.106597.

Clinton, J. F., S. Ceylan, M. van Driel, D. Giardini, S. C. Stähler, M. Bose, C. Charalambous, N. L. Dahmen, A. Horleston, T. Kawamura, *et al.* (2021). The Marsquake catalogue from InSight, sols 0–478, *Phys. Earth Planet. In.* **310,** 106595, doi: 10.1016/j.pepi.2020.106595.

Fourguette, D. C., M. V. Ötügen, L. Larocque, U. Ayaz, and G. Ritter (2012). Optical MEMS-based seismometer, *Proc. of the Monitoring Research Review 2012*, Albuquerque, New Mexico.

Fourguette, D. C., M. V. Otugen, L. M. Larocque, G. A. Ritter, J. J. Meeusen, and T. Loppolo (2014). Whispering-gallery-mode-based seismometer, *US8743372*, available at https://www.osti.gov/doepatents/biblio/1133626 (last accessed August 2021).

Guan, G., S. Arnold, and M. V. Otugen (2006). Temperature measurements using a microoptical sensor based on whispering gallery modes, *AIAA J.* **44,** no. 10, 2385–2389, doi: 10.2514/1.20910.

Ioppolo, T., and M. V. Ötügen (2007). Pressure tuning of whispering gallery mode resonators, *J. Opt. Soc. Am. B* **24,** no. 10, 2721–2726, doi: 10.1364/JOSAB.24.002721.

Ioppolo, T., U. K. Ayaz, and M. V. Ötügen (2009). High-resolution force sensor based on morphology dependent optical resonances of polymeric spheres, *J. Appl. Phys.* **105,** no. 1, 013535, doi: 10.1063/1.3054338.

Ioppolo, T., M. Kozhevnikov, V. Stepaniuk, M. V. Ötügen, and V. Sheverev (2008). Micro-optical force sensor concept based on whispering gallery mode resonators, *Appl. Opt.* **47,** no. 16, 3009–3014, doi: 10.1364/AO.47.003009.

Ioppolo, T., V. Ötügen, D. Fourguette, and L. Larocque (2011). Effect of acceleration on the morphology dependent optical resonances of spherical resonators, *J. Opt. Soc. Am. B* **28,** no. 2, 225–227, doi: 10.1364/JOSAB.28.000225.

Lognonné, P., W. B. Banerdt, D. Giardini, W. T. Pike, U. Christensen, P. Laudet, S. de Raucourt, P. Zweifel, S. Calcutt, M. Bierwirth, *et al.* (2019). SEIS: Insight's seismic experiment for internal structure of Mars, *Space Sci. Rev.* **215,** no. 1, 12, doi: 10.1007/s11214-018-0574-6.

Mansour, G., K. Tsongas, and D. Tzetzis (2016). Investigation of the dynamic mechanical properties of epoxy resins modified with elastomers, *Compos. B Eng.* **94,** 152–159, doi: 10.1016/j.compositesb.2016.03.024.

Namazu, T., Y. Isono, and T. Tanaka (2000). Evaluation of size effect on mechanical properties of single crystal silicon by nanoscale bending test using AFM, *J. Microelectromech. Syst.* **9,** no. 4, 450–459, doi: 10.1109/84.896765.

Park, S. K., and X.-L. Gao (2006). Bernoulli–Euler beam model based on a modified couple stress theory, *J. Micromechan. Microeng.* **16,** no. 11, 2355–2359, doi: 10.1088/09601317/16/11/015.

Rayleigh, L. (1910). CXII. The problem of the whispering gallery, *The London, Edinburgh, and Dublin Phil. Mag. J. Sci.* **20,** no. 120, 1001–1004, doi: 10.1080/14786441008636993.

Rubino, E., and T. Ioppolo (2016). Young's modulus and loss tangent measurement of polydimethylsiloxane using an optical lever, *J. Polym. Sci. B Polym. Phys.* **54,** no. 7, 747–751, doi: 10.1002/polb.23972.

Salameh, E. R., J. D. Silva, M. V. Ötügen, and D. Fourguette (2021). Optical micro-resonator sensor for air velocity measurement, *Proc. Laser Resonators, Microresonators, and Beam Control XXIII*, V. S. Ilchenko, A. M. Armani, J. V. Sheldakova, A. V. Kudryashov, and A. H. Paxton (Editors), Vol. 11672, International Society for Optics and Photonics, SPIE, 89–96, doi: 10.1117/12.2582862.

Soroka, W. W. (1949). Note on the relations between viscous and structural damping coefficients, *J. Aeronaut. Sci.* **16,** no. 7, 409–410, doi: 10.2514/8.11822.

Sumali, H., and T. G. Carne (2007). Air damping on micro-cantilever beams, available at https://www.osti.gov/biblio/1146543-air-damping-micro-cantilever-beams (last accessed March 2021).

Wielandt, E. (2012). Seismic sensors and their calibration, in *New Manual of Seismological Observatory Practice 2 (NMSOP-2)*, P. Bormann (Editor), Deutsches GeoForschungsZentrum GFZ, Germany, Chap. 5, 1–51, doi: 10.2312/GFZ.NMSOP-2_ch5.

Wielandt, E., and G. Streckeisen (1982). The leaf-spring seismometer: Design and performance, *Bull. Seismol. Soc. Am.* **72,** no. 6A, 2349–2367, doi: 10.1785/BSSA07206A2349.

Zumberge, M., J. Berger, W. Hatfield, and E. Wielandt (2018). A three-component borehole optical seismic and geodetic sensor, *Bull. Seismol. Soc. Am.* **108,** no. 4, 2022–2031, doi: 10.1785/0120180045.

Zumberge, M., J. Berger, J. Otero, and E. Wielandt (2010). An optical seismometer without force feedback, *Bull. Seismol. Soc. Am.* **100,** no. 2, 598–605, doi: 10.1785/0120090136.

Zumberge, M., J. Berger, and E. Wielandt (2003). Experiments with an optical seismometer, *AGU Fall Meeting Abstracts*, San Francisco, California, 8–12 December 2003, S52C–0144.

Manuscript received 6 September 2021
Published online 26 January 2022